Research Square

Preprints are preliminary reports that have not undergone peer review.
They should not be considered conclusive, used to inform clinical practice,
or referenced by the media as validated information.

Temporal modulation of nonlinear Lagrangian dynamics and finite-time stretching in incompressible flows

Weiqi Wen

7111167541@edu.k.u-tokyo.ac.jp

The University of Tokyo

Hiroshi Kori

The University of Tokyo

Research Article

Keywords:

Posted Date: November 6th, 2026

DOI: https://doi.org/10.21203/rs.3.rs-11387023/v1

License: This work is licensed under a Creative Commons Attribution 4.0 International License.
Read Full License

Additional Declarations: No competing interests reported.

Temporal modulation of nonlinear Lagrangian dynamics and finite-time stretching in incompressible flows

Weiqi Wen[1*] and Hiroshi Kori[1]

[1]Department of Complexity Science and Engineering, The University of Tokyo, Kashiwa, Chiba, 277-8561, Japan.

*Corresponding author. E-mail: 7111167541@edu.k.u-tokyo.ac.jp;

Abstract

External temporal signals can alter flow deformation and particle transport, yet how changes in signal characteristics are transmitted into Eulerian and Lagrangian responses remains unclear. Here, a temporal input signal modulates the spatial velocity field, and its modulation intensity is quantified by the phase modulation rate (PMR), defined as the standard deviation of the input time derivative. Theoretical derivation shows that signal evolution enters the velocity-gradient tensor, establishing a direct mechanism for input-induced Eulerian deformation. We characterize the resulting response using Eulerian activity, measured by velocity-fluctuation energy and strain-rate magnitude, and finite-time Lagrangian stretching, quantified by the finite-time Lyapunov exponent (FTLE). To examine this framework, a divergence-free two-dimensional multiscale flow is constructed using a phase-modulated stream function and driven by Periodic, Ornstein–Uhlenbeck (OU), Lorenz, and smoothed OU inputs. Across all forcing families, increasing PMR produces a comparatively regular enhancement of Eulerian activity. FTLE statistics show an overall increase with PMR, accompanied by local non-monotonic variations arising from strain–rotation interactions and separation-direction dynamics. The upper-tail FTLE statistics, particularly P95 and P99, show stronger responses to temporal modulation. Refined OU scans confirm the response trends across different baseline correlation times, while Navier–Stokes CFD simulations reproduce the same modulation-dependent progression. These results characterize the relationship between temporal input modulation, Eulerian deformation, and finite-time Lagrangian stretching, with PMR serving as a common measure for comparing responses across the forcing families examined.

Keywords: Temporal modulation, Phase modulation rate, Finite-time Lyapunov exponent, Lagrangian dynamics, Eulerian deformation

1 Introduction

Temporal variability can fundamentally reorganize how material is transported by a flow, even when its underlying spatial structure remains comparatively simple. Many natural and engineered flows are time dependent because of externally imposed actuation, environmental fluctuations, active control, or stochastic disturbances, while others exhibit intrinsic temporal variability. From a dynamical-systems perspective, the resulting fluid-particle motion can be formulated as a non-autonomous system governed by the time-dependent velocity field. Aref [1] established this perspective in the context of chaotic advection, showing that relatively simple time-dependent

two-dimensional flows can generate chaotic particle trajectories. Ottino [2] subsequently connected chaotic advection with stretching, material deformation, and mixing, while Aref et al. [3] later reviewed its broader development at the interface of fluid mechanics and nonlinear dynamics. Experimental work by Solomon and Gollub [4] further demonstrated that time-periodic convection can produce chaotic particle transport and strongly enhance transport across otherwise weakly connected flow regions.

The response of an unsteady flow can be described from complementary Eulerian and Lagrangian perspectives. In an Eulerian description, flow quantities are represented as fields evaluated at fixed spatial locations, whereas the Lagrangian description follows fluid particles and material elements through the evolving flow. Local Eulerian diagnostics can therefore characterize the instantaneous state and deformation activity of the velocity field, while Lagrangian measures reflect material evolution accumulated along trajectories. Voth, Haller, and Gollub [5] experimentally reconstructed time-dependent stretching fields from particle trajectories, demonstrating the Lagrangian character of material deformation. Haller [6] further showed that finite-time material structures can be characterized using dynamical information sampled along fluid trajectories. Within this framework, Shadden, Lekien, and Marsden [7] developed FTLE-based diagnostics for finite-time trajectory separation, while Haller [8] later provided a broader theoretical synthesis of Lagrangian coherent structures and finite-time transport.

Finite-time material deformation depends on the time history of local kinematics sampled along fluid trajectories, and several studies have examined the mechanisms involved in this evolution. Girimaji and Pope [9] investigated infinitesimal material-element deformation in isotropic turbulence and showed that vorticity and non-persistent straining influence the growth of material lines and surfaces. Dresselhaus and Tabor [10] subsequently derived the evolution of material-element alignment relative to the principal strain directions, identifying the roles of local angular velocity and rotation of the strain axes in the alignment process. Lapeyre [11] further examined finite-time Lyapunov vectors in terms of the competition between effective rotation and strain, while Thiffeault [12] related material-line stretching to the evolution of line geometry and curvature in chaotic flows. Experimentally, Kelley and Ouellette [13] separated stretching and folding in a two-dimensional chaotic flow and showed that their relative contributions evolve differently in space and time. These studies provide a theoretical and experimental basis for considering strain, rotation, alignment, and kinematic history in analyses of finite-time material deformation.

Alongside these studies of finite-time deformation mechanisms, a complementary body of work has examined how temporal characteristics of a flow or its forcing influence flow organization and transport. Aref and Balachandar [14] showed that slow temporal modulation of a Stokes flow can generate chaotic particle motion, while Rom-Kedar, Leonard, and Wiggins [15] demonstrated that an oscillatory strain field can alter transport structures in an unsteady vortical flow. Kuczaj et al. [16] identified frequency-dependent turbulent responses under periodically modulated forcing, and Wang et al. [17] examined the influence of forcing frequency on chaotic advection and mixing in a two-dimensional cavity. In natural and environmental systems, Trefry et al. [18] demonstrated that cyclical forcing can generate complex Lagrangian transport in groundwater flows. More recent studies have extended these questions to heterogeneous poroelastic media [19], time-dependent oceanic transport [20], and temporally modulated turbulent convection [21]. Tajima and Dentz [22] investigated transiently forced transport and mixing in heterogeneous aquifers using particle-based and dynamical diagnostics, while Kim et al. [23] recently combined Eulerian velocity and vorticity measurements with FTLE-based Lagrangian analysis in pulsatile jets. Together, these studies illustrate the sensitivity of flow organization and material transport to temporal variation across a broad range of physical configurations.

Collectively, existing studies provide substantial evidence that temporal variation can influence both Eulerian flow behavior and Lagrangian transport, with forcing amplitude, frequency, and protocol serving as useful control parameters in different systems. These findings motivate a related question: whether the temporal input itself can be characterized by a compact quantitative descriptor that provides a common basis for

comparing Eulerian and finite-time Lagrangian responses. More specifically, it is of interest to determine whether such a signal-derived measure can organize response trends across qualitatively different input families and how this organization is reflected at the velocity-gradient and finite-time particle-transport levels.

Motivated by these considerations, the present study considers an unsteady incompressible flow driven by controlled temporal modulation and focuses on the dynamical pathway from the input signal to local velocity-gradient activity and finite-time particle stretching. Rather than treating the Eulerian and Lagrangian responses as independent diagnostics, the analysis examines them within a common input-modulation framework, allowing their respective relationships with the temporal forcing to be compared directly.

The remainder of this paper is organized as follows. Section 2 develops the theoretical formulation of input-modulated flow dynamics, including the definition of PMR, its relation to Eulerian velocity-gradient dynamics, and the strain–rotation–alignment dynamics underlying finite-time stretching. Section 3 introduces the numerical model and methodology, including the stream function formulation, Eulerian activity measures, and FTLE calculation. Section 4 presents the modulation-dependent Eulerian and Lagrangian responses, including extreme stretching behavior and their consistency across parameter scans and input families. Section 5 presents the Navier–Stokes validation, Section 6 discusses the physical implications, and Section 7 summarizes the main conclusions.

2 Theoretical framework

2.1 Flow and phase modulation rate

We consider a two-dimensional velocity field $\mathbf{u}$ satisfying the incompressibility condition

$$\nabla \cdot \mathbf{u} = \frac{\partial u}{\partial x} + \frac{\partial v}{\partial y} = 0. \tag{1}$$

To satisfy this condition [1], the velocity field is constructed using a stream function $\psi(x, y, t)$, where:

$$u = \frac{\partial \psi}{\partial y}, v = -\frac{\partial \psi}{\partial x}. \tag{2}$$

The stream function is written as the sum of a steady component and an input-modulated component,

$$\psi(x, y, t) = \psi_0(x, y) + \psi_{\text{in}} \left[x, y, f\left(t - \frac{x}{U_0} \right) \right], \tag{3}$$

where ψ_0 denotes the steady component, ψ_{in} denotes the input-modulated component, $f(t)$ is the external temporal input, and $U_0$is the downstream convection velocity.

The input is introduced with a streamwise-dependent time delay, $f\left(t - x/U_0\right)$. This construction allows the temporal variation of the input to enter the spatial dependence of the flow. By the chain rule,

$$\frac{\partial}{\partial x} f\left(t - \frac{x}{U_0} \right) = -\frac{1}{U_0} \frac{df}{dt}\left(t - \frac{x}{U_0} \right), \tag{4}$$

To quantify the overall intensity of this temporal variation, we define the phase modulation rate (PMR) as

$$PMR = std\left(\frac{df}{dt} \right). \tag{5}$$

For the discrete signals used in the numerical simulations, PMR is evaluated as

$$PMR_{\Delta t} = std\left(\frac{f_{j+1} - f_j}{\Delta t} \right), \tag{6}$$

where Δt is the sampling interval. The same temporal resolution is used for all input signals to ensure consistent evaluation.

PMR therefore represents the overall temporal modulation rate of the input signal. The effect of this input modulation on the velocity-gradient field is derived in the following section.

2.2 Eulerian velocity-gradient dynamics

The phase-modulated stream function introduced in Sect. 2.1 determines the velocity field through

$$u = \frac{\partial \psi}{\partial y}, v = -\frac{\partial \psi}{\partial x}. \tag{7}$$

For $\psi(x, y, t)$, the velocity components become

$$u = \psi_{0,y} + \psi_{\text{in},y}, \tag{8}$$

$$v = -\psi_{0,x} - \psi_{\mathrm{in},x} + \frac{1}{U_0}\psi_{\mathrm{in},f}\frac{df}{dt}. \tag{9}$$

Here, subscripts denote partial derivatives with respect to the corresponding variables. For clarity, the time derivatives of f are evaluated at $t-x/U_0$, although this argument is omitted in the following equations.

The local velocity-gradient tensor is defined as

$$\nabla\mathbf{u} = \begin{bmatrix} u_x & u_y \\ v_x & v_y \end{bmatrix}. \tag{10}$$

Applying the chain rule gives

$$\begin{cases} u_x = \psi_{0,xy} + \psi_{\mathrm{in},xy} - \dfrac{1}{U_0}\psi_{\mathrm{in},yf}\dfrac{df}{dt}, \\ u_y = \psi_{0,yy} + \psi_{\mathrm{in},yy}, \\ v_y = -u_x, \\ v_x = -\psi_{0,xx} - \psi_{\mathrm{in},xx} + \dfrac{2}{U_0}\psi_{\mathrm{in},xf}\dfrac{df}{dt} \\ \qquad - \dfrac{1}{U_0^2}\psi_{\mathrm{in},ff}\left(\dfrac{df}{dt}\right)^2 - \dfrac{1}{U_0^2}\psi_{\mathrm{in},f}\dfrac{d^2f}{dt^2}. \end{cases} \tag{11}$$

Equation (11) shows that the temporal input affects the local velocity gradient through several terms. The components u_x and v_y contain contributions proportional to $\frac{df}{dt}$, while v_x additionally contains terms involving $\left(\frac{df}{dt}\right)^2$ and $\frac{d^2f}{dt^2}$. The component u_y is affected mainly through the instantaneous value of f.

Therefore, changes in the temporal input can modify both the magnitude and the orientation of the local velocity-gradient tensor. PMR characterizes the intensity of input-rate variation entering the velocity-gradient dynamics. The resulting gradient field also depends on the instantaneous input, higher-order temporal derivatives, and the spatial structure of the stream function.

This result provides the theoretical connection between the input signal and the Eulerian deformation of the flow field. The relation between the velocity-gradient dynamics and finite-time particle stretching is considered in the next section.

2.3 Finite-time stretching

The velocity-gradient tensor derived in Sect. 2.2 determines the local evolution of neighboring particle trajectories. Consider two particles with positions $\mathbf{p}(t)$ and $\mathbf{p}(t) + \delta\mathbf{p}(t)$, where $\delta\mathbf{p}$ is an infinitesimal separation vector. Their separation satisfies

$$\frac{d\delta\mathbf{p}}{dt} = \mathbf{u}\left(\mathbf{p} + \delta\mathbf{p}, t\right) - \mathbf{u}\left(\mathbf{p}, t\right). \tag{12}$$

For sufficiently small $\| \delta\mathbf{p} \|$, shown in Fig. 1(a,b) a first-order expansion gives

$$\frac{d\delta\mathbf{p}}{dt} = \nabla\mathbf{u}\left(\mathbf{p}, t\right)\, \delta\mathbf{p}. \tag{13}$$

Equation (13) shows that the local velocity-gradient tensor determines the linearized evolution of neighboring particle separation. This provides the connection between the Eulerian velocity field and Lagrangian stretching.

For an initial position $\mathbf{p}_0$ and a finite integration time $T > 0$, the finite-time Lyapunov exponent (FTLE) is defined as the maximum logarithmic growth rate of an infinitesimal separation [7, 8],

$$\mathrm{FTLE} = \frac{1}{T}\ln\left[\max_{\delta\mathbf{p}(t_0)\neq 0}\frac{\| \delta\mathbf{p}\left(t_0+T\right) \|}{\| \delta\mathbf{p}\left(t_0\right) \|}\right]. \tag{14}$$

FTLE therefore measures the maximum average exponential separation rate of initially neighboring trajectories over the prescribed finite time interval. Larger positive FTLE values indicate stronger finite-time stretching. This definition is consistent with the use of finite-time Lyapunov exponents in nonlinear-dynamics studies.

To identify the contributions of local deformation and rotation, the velocity-gradient tensor is decomposed as

$$\nabla\mathbf{u} = \mathbf{S} + \mathbf{\Omega}, \tag{15}$$

$$\mathbf{S} = \frac{1}{2}(\nabla\mathbf{u} + \nabla\mathbf{u}^T), \qquad \mathbf{\Omega} = \frac{1}{2}(\nabla\mathbf{u} - \nabla\mathbf{u}^T). \tag{16}$$

Let the separation magnitude be $\| \delta\mathbf{p} \|$, and define the unit separation direction as

$$\mathbf{n} = \frac{\delta\mathbf{p}}{\| \delta\mathbf{p} \|}. \tag{17}$$

Using Eq. (13), the instantaneous logarithmic stretching rate is

$$\frac{d}{dt} ln \| \delta\mathbf{p} \| = \mathbf{n}^T\mathbf{S}\mathbf{n}. \tag{18}$$

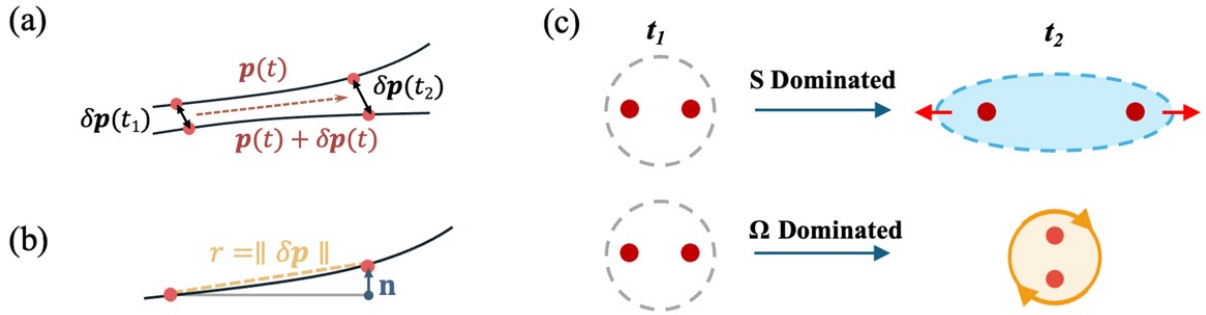


Fig. 1 Schematic of finite-time particle separation and the distinct roles of strain and rotation. (a) Evolution of the separation vector $\delta\mathbf{p}$ between two neighboring trajectories from t_1 to t_2. (b) Decomposition of the separation vector into its magnitude $r = \|\delta\mathbf{p}\|$ and orientation $\mathbf{n}$. (c) Conceptual comparison between strain-dominated $\mathbf{S}$ deformation, which promotes stretching, and rotation-dominated $\mathbf{\Omega}$ motion, which primarily changes the orientation of the separation vector

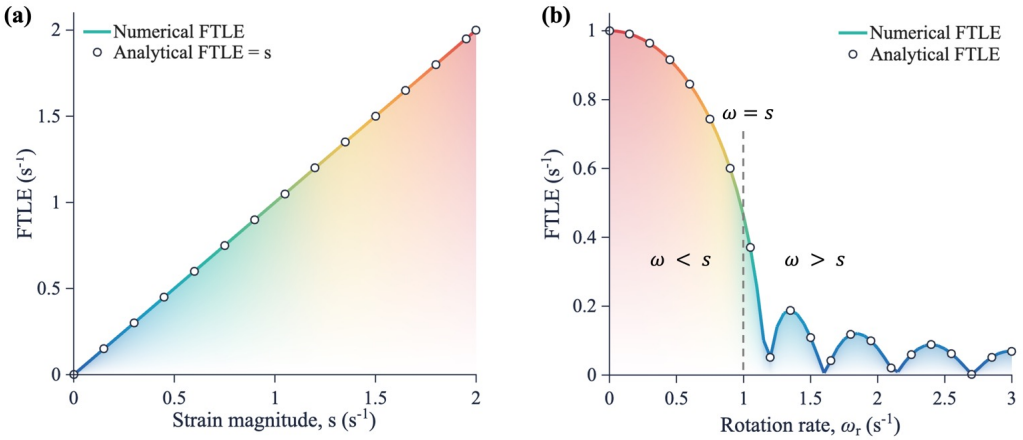


Fig. 2 Analytical and numerical illustration of strain–rotation effects on finite-time stretching. (a) For pure strain, the numerical FTLE increases linearly with the strain-rate parameter s and coincides with the analytical relation $FTLE = s$. (b) For fixed $s = 1$, the rotation-rate scan spans $\omega < s$, $\omega = s$, and $\omega > s$, corresponding to the strain-dominated hyperbolic branch, the critical case, and the rotation-dominated oscillatory branch of the piecewise expression for $H(T)$, respectively. In the oscillatory regime, finite-time cancellation produces the repeated low-FTLE states.

Because $\mathbf{\Omega}$ is antisymmetric, $\mathbf{n}^T\mathbf{\Omega}\mathbf{n} = 0$.

Therefore, $\mathbf{\Omega}$ does not directly change the instantaneous separation magnitude. The instantaneous stretching rate is determined by the projection of $\mathbf{S}$ onto the current separation direction.

However, the separation direction also evolves. Differentiating Eq. (17) gives

$$\frac{d\mathbf{n}}{dt} = \mathbf{S}\mathbf{n} - \left(\mathbf{n}^T\mathbf{S}\mathbf{n}\right)\mathbf{n} + \mathbf{\Omega}\mathbf{n}. \tag{19}$$

Equation (19) shows that rotation affects stretching indirectly by changing the separation direction $\mathbf{n}(t)$, which in turn modifies the subsequent strain projection $\mathbf{n}^T\mathbf{S}\mathbf{n}$. Thus, finite-time stretching is governed by strain and indirectly modulated by rotation through the evolving separation direction.

The geometric interpretation of this mechanism is illustrated in Fig. 1(c). The strain-rate tensor provides extensional and compressional directions, while rotation changes the orientation of the particle-separation vector relative to these directions.

Integrating Eq. (18) over the finite interval gives

$$\mathrm{FTLE} = \max_{\mathbf{n}(t_0)} \left[\frac{1}{T} \int_{t_0}^{t_0+T} \mathbf{n}^T(t)\mathbf{S}(t)\mathbf{n}(t)\, dt \right]. \tag{20}$$

Equation (20) expresses finite-time stretching as the accumulated strain projection along the evolving separation direction.

To isolate this mechanism, we consider a simple two-dimensional incompressible linear system,

$$\mathbf{S} = \begin{bmatrix} s & 0 \\ 0 & -s \end{bmatrix}, \mathbf{\Omega} = \begin{bmatrix} 0 & -\omega \\ \omega & 0 \end{bmatrix}, \tag{21}$$

where s is the strain-rate parameter and ω is the rotation rate. The separation equation becomes

$$\frac{d\delta\mathbf{p}}{dt} = \begin{bmatrix} s & -\omega \\ \omega & -s \end{bmatrix} \delta\mathbf{p}. \tag{22}$$

When $\omega = 0$, the maximizing separation direction remains aligned with the extensional direction of $\mathbf{S}$, giving FTLE $= s$. The numerical results reproduce this analytical relation, as shown in Fig. 2(a). This case provides a reference for sustained stretching without rotation.

With s fixed, increasing ω changes the competition between strain and rotation without changing the strain-rate tensor itself. Figure 2(b) therefore scans continuously across $\omega < s$, $\omega = s$, and $\omega > s$, allowing the finite-time response on both sides of the critical condition to be compared directly.

For the system in Eq. (22), differentiating once more gives

$$\frac{d^2\delta\mathbf{p}}{dt^2} = \begin{bmatrix} s & -\omega \\ \omega & -s \end{bmatrix}^2 \delta\mathbf{p} = \left(s^2 - \omega^2\right) \delta\mathbf{p}. \tag{23}$$

The corresponding finite-time stretching can be obtained analytically. Let $\mathbf{F}(T)$ denote the deformation gradient, defined by $\mathbf{F}(T) = \exp[(\mathbf{S} + \mathbf{\Omega})T]$. We further define $H(T) = \frac{1}{2}\,\mathrm{tr}[\mathbf{F}^T(T)\mathbf{F}(T)]$. For this incompressible system, $\det[\mathbf{F}^T(T)\mathbf{F}(T)] = 1$. The FTLE can therefore be expressed as

$$\mathrm{FTLE}(T) = \frac{1}{2T}\,\mathrm{arcosh}\,H(T). \tag{24}$$

The piecewise form of $H(T)$ follows directly from Eq. (23) and is

$$H(T) = \begin{cases} 1 + \frac{2s^2}{s^2-\omega^2}\sinh^2\left(\sqrt{s^2-\omega^2}\,T\right), & s^2 > \omega^2, \\ 1 + 2s^2T^2, & s^2 = \omega^2, \\ 1 + \frac{2s^2}{\omega^2-s^2}\sin^2\left(\sqrt{\omega^2-s^2}\,T\right), & s^2 < \omega^2. \end{cases} \tag{25}$$

Equation (25) distinguishes two dynamical regimes separated by the critical case $\omega = s$. For $\omega < s$, the hyperbolic branch corresponds to a strain-dominated regime in which sustained finite-time stretching remains possible. At $\omega = s$, the system reaches the limiting case between hyperbolic and oscillatory behavior. For $\omega > s$, the trigonometric branch defines a rotation-dominated oscillatory regime, producing the non-monotonic FTLE response shown in Fig. 2(b). In this regime, complete finite-time cancellation occurs when

$$\sqrt{\omega^2 - s^2}\,T = n\pi, \quad n = 1, 2, 3, \ldots \tag{26}$$

for which $H(T) = 1$ and therefore FTLE $= 0$. The corresponding rotation rates are

$$\omega_n = \sqrt{s^2 + \left(\frac{n\pi}{T}\right)^2}. \tag{27}$$

For $s = 1$ and $T = 5$, these analytical locations agree with the repeated low-FTLE positions in Fig. 2(b). Thus, the three branches of $H(T)$ provide a direct analytical interpretation of the rotation-rate scan: sustained stretching for $\omega < s$, the critical case at $\omega = s$, and oscillatory stretching–compression cancellation for $\omega > s$.

The above analysis shows that finite-time stretching is determined by both strain and directional dynamics. Increasing strain increases the available stretching capacity, whereas rotation changes the separation direction relative to the extensional strain direction. In the rotation-dominated regime, repeated reorientation can produce alternating stretching and compression, leading to partial or complete cancellation over a finite interval. This mechanism provides a theoretical explanation for the local decreases and fluctuations of FTLE observed later in the full flow simulations.

3 Numerical method

3.1 Setup

A specific three-mode stream function was used to implement the general phase-modulated flow introduced in Sect. 2. Fourier-mode-based kinematic constructions have long been used to generate divergence-free, time-dependent velocity fields

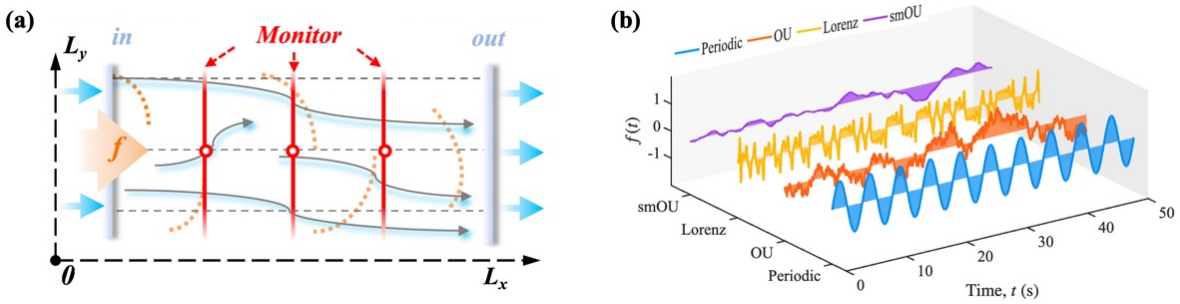


Fig. 3 Computational configuration and representative temporal input signals. (a) Two-dimensional flow domain showing the inlet, center, and outlet monitoring locations. (b) Representative normalized Periodic $T_{\mathrm{p}} = 5$, OU $T_{\mathrm{OU}} = 2$, Lorenz $\rho = 28$, and $T_{\mathrm{sm}} = 5$ temporal inputs used in the simulations

with prescribed spatial and temporal structure [24, 25]. In the present study, a small number of modes is deliberately retained to construct a controlled multiscale incompressible flow rather than to reproduce a prescribed turbulence spectrum.

For the numerical implementation, the base-flow component is written as

$$\psi_0(x, y) = U_0 y, \tag{28}$$

while the input-modulated component is constructed from three spatial modes,

$$\psi_{\mathrm{in}}(x, y, t) = \sum_{n=1}^{3} \psi_n(x, y, t). \tag{29}$$

with

$$\psi_n(x, y, t) = A_n \sin\left[k_{x,n} x + f\left(t - \frac{x}{U_0}\right)\right] \times \sin(k_{y,n} y). \tag{30}$$

The three modes represent large-, intermediate-, and smaller-scale vortical structures. The velocity field is obtained from

$$u = \frac{\partial \psi}{\partial y}, v = -\frac{\partial \psi}{\partial x}, \tag{31}$$

The streamwise wavenumbers are

$$k_{x,n} = \left\{\frac{2\pi}{L_x}, \frac{4\pi}{L_x}, \frac{8\pi}{L_x}\right\}, \tag{32}$$

corresponding to streamwise wavelengths L_x, $L_x/2$, and $L_x/4$. The wall-normal wavenumbers are

$$k_{y,n} = \frac{n\pi}{L_y}, n = 1, 2, 3. \tag{33}$$

Because $\sin(k_{y,n} y) = 0$ at $y = 0$ and $y = L_y$, the resulting wall-normal velocity satisfies the no-penetration condition at the upper and lower boundaries. This construction does not impose a no-slip condition.

To avoid an artificial increase in the nominal velocity scale of the higher-wavenumber modes, the stream function amplitudes are normalized as

$$A_n = \frac{\alpha \mid U_0 \mid}{\sqrt{k_{x,n}^2 + k_{y,n}^2}}, \tag{34}$$

where α controls the perturbation strength relative to the background flow. This normalization gives the three modes comparable characteristic velocity scales of order αU_0.

The computational domain is $0 \le x \le L_x$ and $0 \le y \le L_y$, with $L_x = 10$ and $L_y = 1$. A uniform 200×50 grid is used with $\Delta t = 0.02$ s and $T_{\mathrm{total}} = 50$ s. The background velocity is $U_0 = 1$, the perturbation strength is $\alpha = 0.10$. The computational configuration is illustrated in Fig. 3(a).

Four types of unsteady inputs are considered: periodic, Ornstein–Uhlenbeck (OU), Lorenz, and smoothed OU signals.

The periodic input is defined as

$$f(t) = \sin\left(\frac{2\pi t}{T_{\mathrm{p}}}\right), \tag{35}$$

where $T_{\mathrm{p}}$is the forcing period. The OU input is generated from the Ornstein–Uhlenbeck process [26],

$$df = -\frac{1}{T_{\mathrm{OU}}} f\, dt + \sigma_{\mathrm{OU}}\, dW_t, \tag{36}$$

where T_{OU} is the correlation time scale, W_t is a Wiener process, and $\sigma_{\mathrm{OU}} = 1$. Its PMR is evaluated from the discrete signal according to Sect. 2.1.

The Lorenz input is taken from the x-component of

$$\begin{aligned} \tfrac{dx}{dt} &= \sigma(y - x), \\ \tfrac{dy}{dt} &= x(\rho - z) - y, \\ \tfrac{dz}{dt} &= xy - \beta z. \end{aligned} \tag{37}$$

with $\sigma = 10$, $\beta = 8/3$, and varying ρ [27].

The smOU input is obtained by applying a moving average to an OU sequence,

$$f_{smOU,j} = \frac{1}{M} \sum_{q=0}^{M-1} f_{OU,j-q}, M \simeq \frac{T_{\mathrm{sm}}}{\Delta t}. \tag{38}$$

Before entering the stream function, all unsteady inputs are centered and normalized as

$$\langle f \rangle = 0, std(f) = 1. \tag{39}$$

Representative normalized signals are shown in Fig. 3(b). The parameter variations used for the baseline cases and subsequent modulation scans are introduced together with the corresponding results in Sect. 4.

3.2 Eulerian measures

Two complementary quantities are used to characterize the Eulerian response of the flow: the two-dimensional velocity-fluctuation energy $k_{2\mathrm{D}}$ and the strain-rate magnitude $|S|$. The former measures the intensity of unsteady velocity fluctuations, whereas the latter quantifies the local deformation rate.

The time-averaged velocity field is calculated over the post-transient interval $t_s \leq t \leq t_e$, with $t_s = 15$ and $t_e = 50$,

$$\begin{aligned} \bar{u}(x, y) &= \tfrac{1}{t_e - t_s} \textstyle\int_{t_s}^{t_e} u(x, y, t)\, dt, \\ \bar{v}(x, y) &= \tfrac{1}{t_e - t_s} \textstyle\int_{t_s}^{t_e} v(x, y, t)\, dt. \end{aligned} \tag{40}$$

The velocity fluctuations are defined as

$$u^{'} = u - \bar{u}, v^{'} = v - \bar{v}. \tag{41}$$

The two-dimensional velocity-fluctuation energy is

$$k_{2\mathrm{D}} = \frac{1}{2} \left(u^{'2} + v^{'2} \right). \tag{42}$$

Here, $k_{2\mathrm{D}}$is used as a measure of local unsteady velocity-fluctuation intensity rather than as a full three-dimensional turbulent kinetic energy. This definition is consistent with the quantity used in the numerical analysis.

The second measure is based on the strain-rate tensor introduced in Sect. 2.3,

$$\mathbf{S} = \frac{1}{2} \left(\nabla \mathbf{u} + \nabla \mathbf{u}^T \right), \tag{43}$$

with the strain-rate magnitude

$$|S| = \sqrt{2\, \mathbf{S} : \mathbf{S}} = \sqrt{2S_{xx}^2 + 2S_{yy}^2 + 4S_{xy}^2}. \tag{44}$$

The quantity $|S|$measures local deformation while excluding the rigid-body rotation contained in the antisymmetric part of the velocity gradient. It is therefore consistent with the strain–rotation framework developed in Sect. 2.3.

For each case, $k_{2\mathrm{D}}$ and $|S|$ are averaged over the full computational domain and over $t \geq 15$ s to obtain the primary Eulerian activity measures. Their downstream persistence is additionally examined at $x = 2$, 5, and 8. Local probes are centered at $y = 0.5L_y$ with radius $r = 0.1$, and cross-sectional statistics are evaluated at the same streamwise locations. These monitoring positions are shown in Fig. 3(a).

3.3 Lagrangian dynamics and FTLE

Lagrangian dynamics are quantified using the finite-time Lyapunov exponent (FTLE), which measures the maximum finite-time stretching of initially neighboring passive tracers. The particles are advected by the velocity field and do not affect the flow.

For each initial seed $\mathbf{p}_0 = (x_0, y_0)$, four neighboring particles are placed at

$$\begin{aligned} \mathbf{p}_{\pm x}(t_0) &= (x_0 \pm \delta_0, y_0), \\ \mathbf{p}_{\pm y}(t_0) &= (x_0, y_0 \pm \delta_0), \end{aligned} \tag{45}$$

with

$$\delta_0 = \frac{1}{2} \min(\Delta x, \Delta y). \tag{46}$$

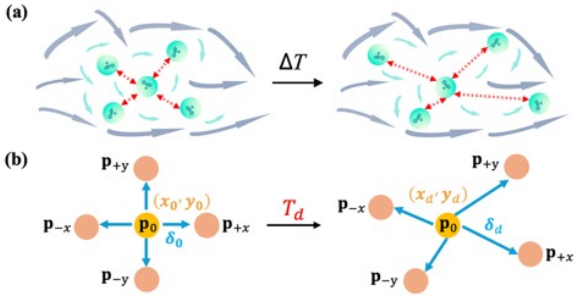


Fig. 4 Schematic of finite-time Lagrangian deformation and FTLE calculation. (a) Deformation of neighboring particles over a finite time interval ΔT. (b) Four particles are initialized around the reference particle p_0 with perturbation δ_0 and integrated over T_d. Their final positions are used to estimate the flow-map Jacobian by centered finite differences and subsequently compute the Cauchy–Green tensor and FTLE

The initial seed points are sampled every eighth grid point in the x direction and every fourth grid point in the y direction. Only boundary-safe seeds that can be tracked over the complete integration interval are retained. In the present calculations, the FTLE integration time is $T_\mathrm{d} = 2.0$ s, and particles are released at $t_0 = 15, 20, \ldots, 40$s. These settings follow the final numerical implementation.

After advection over T_d, the deformation gradient is estimated from the four neighboring trajectories using centered finite differences [7, 28],

$$\mathbf{F} \approx \frac{1}{2\delta_0} \begin{bmatrix} [\mathbf{p}_{+x}(t_0+T_\mathrm{d}) - \mathbf{p}_{-x}(t_0+T_\mathrm{d})]^T \\ [\mathbf{p}_{+y}(t_0+T_\mathrm{d}) - \mathbf{p}_{-y}(t_0+T_\mathrm{d})]^T \end{bmatrix}^T . \tag{47}$$

This numerical construction is illustrated in Fig. 4.

The FTLE is then calculated from the maximum singular stretching of $\mathbf{F}$,

$$\begin{aligned} \mathrm{FTLE} &= \tfrac{1}{T_\mathrm{d}} \ln \sigma_{\max}(\mathbf{F}) \\ &= \tfrac{1}{2T_\mathrm{d}} \ln \lambda_{\max}\left(\mathbf{F}^T\mathbf{F}\right). \end{aligned} \tag{48}$$

This definition is consistent with the finite-time stretching formulation introduced in Sect. 2.3. The numerical implementation explicitly constructs the deformation gradient from four neighboring trajectories and evaluates the maximum eigenvalue of $\mathbf{F}^T\mathbf{F}$.

For each case, all valid FTLE samples from the seed positions and release times are combined into one distribution. Four statistics are used in the main analysis [29]. Mean FTLE represents the average finite-time stretching over all valid samples. P90 FTLE is the 90th percentile, P95 FTLE is the 95th percentile and is used to characterize strong-stretching events in the upper 5% of the distribution. P99 FTLE is the 99th percentile and represents extreme stretching in the upper 1%. These statistics distinguish changes in the typical Lagrangian response from changes in rare high-stretching events.

4 Results

4.1 Eulerian activity

We first examine how temporal input modulation affects the Eulerian activity of the flow. The modulation-strength scan was performed within four input families. The baseline cases were defined by $T_\mathrm{p} = 1.5, 2, 3, 5, 10$ for Periodic inputs; $T_\mathrm{OU} = 0.5, 1, 2, 4, 8$ for OU inputs; $\rho = 20, 22, 28, 35, 40$ for Lorenz inputs; and $T_\mathrm{sm} = 1, 2, 3, 5, 8$ for smOU inputs. For each baseline signal, the normalized input was rescaled as $f_I(t) = If(t)$, with $I = 0.5, 1, 2, 3, 4$. Here I is a dimensionless amplitude scaling factor that preserves the waveform and characteristic time scale. PMR was evaluated separately for each rescaled signal. This procedure preserves the waveform and characteristic time scale while systematically changing PMR within each baseline case.

Across all four input families, increasing PMR produces a clear and smooth increase in both the whole-field velocity-fluctuation energy $\langle k_\mathrm{2D}\rangle_{x,y,t}$ and the strain-rate magnitude $\langle|S|\rangle_{x,y,t}$, as shown in Fig. 5. The same tendency is observed across the different baseline cases within each family. Both $\langle|S|\rangle_{x,y,t}$ and $\langle k_\mathrm{2D}\rangle_{x,y,t}$ increase approximately linearly with PMR over most of the examined range. These tendencies are also observed in the finer OU scans, supporting their consistency across different sampling resolutions of the modulation-strength parameter.

These results are consistent with the theoretical relation derived in Sect. 2.2. The temporal variation of the input enters the velocity-gradient field directly through terms involving df/dt, providing a mechanism through which stronger temporal modulation can enhance Eulerian activity. Consistent with this mechanism, both velocity-fluctuation energy and strain-rate

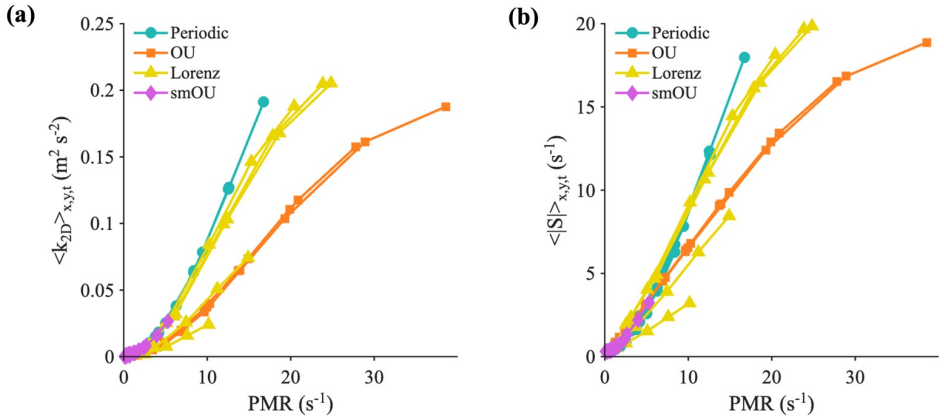


Fig. 5 Whole-field Eulerian response to phase modulation rate (PMR). (a) Whole-field and time-averaged two-dimensional velocity-fluctuation energy, k_{2D}. (b) mean strain-rate magnitude, $|S|$, as functions of PMR for the Periodic, OU, Lorenz, and smOU input families

magnitude exhibit clear positive responses to increasing PMR.

The detailed response levels vary among input families, reflecting differences in their temporal structures. Nevertheless, increasing PMR consistently enhances both velocity fluctuations and local deformation within each family, establishing PMR as a common measure for organizing the Eulerian response.

4.2 Lagrangian response

We next examine how the increase in temporal modulation is transferred to finite-time Lagrangian stretching. The same modulation-strength scans defined in Sect. 4.1 are used, and the response is quantified by the Mean, P90, P95, and P99 FTLE statistics.

Across the Periodic, OU, Lorenz, and smOU families, higher PMR is generally associated with larger FTLE. The increase is particularly clear in the upper part of the FTLE distribution, where P95 and P99 respond more strongly than the mean. Stronger temporal modulation therefore produces larger changes in the upper-tail FTLE statistics than in the mean, as shown in Fig. 6.

Individual amplitude scans show local plateaus, decreases, and fluctuations as PMR increases. Such behavior occurs in several Periodic, OU, and Lorenz cases and is more pronounced in the upper-tail FTLE statistics (P95 and P99). At lower PMR, the positive response is generally clearer, whereas local non-monotonicity becomes more frequent as the modulation level increases.

This behavior differs from the comparatively smooth Eulerian response observed in Sect. 4.1. Increasing PMR produces a regular increase in k_{2D} and $|S|$, whereas the corresponding Lagrangian instability responds through finite-time accumulation along particle trajectories.

The difference can be understood using the mechanism derived in Sect. 2.3. A larger strain-rate magnitude increases the local capacity for stretching, whereas FTLE depends on the accumulated effective stretching $\mathbf{n}^T\mathbf{S}\mathbf{n}$ along the trajectory. Rotation changes the separation direction $\mathbf{n}(t)$ and therefore changes its alignment with the extensional directions of $\mathbf{S}$. Stretching and compression can consequently partially cancel over the finite integration time, producing local variations in FTLE even as Eulerian deformation activity increases. This explains why FTLE can exhibit local non-monotonic variations even when Eulerian deformation increases smoothly with PMR.

4.3 Extreme behavior

The FTLE response is strongly heterogeneous across particle trajectories. To identify which part of the distribution is most affected by temporal modulation, we further examine the full FTLE distributions and their upper tails.

As shown in Fig. 7, most FTLE samples remain within a relatively low or moderate range, while a much smaller fraction extends to substantially larger values. The resulting distributions

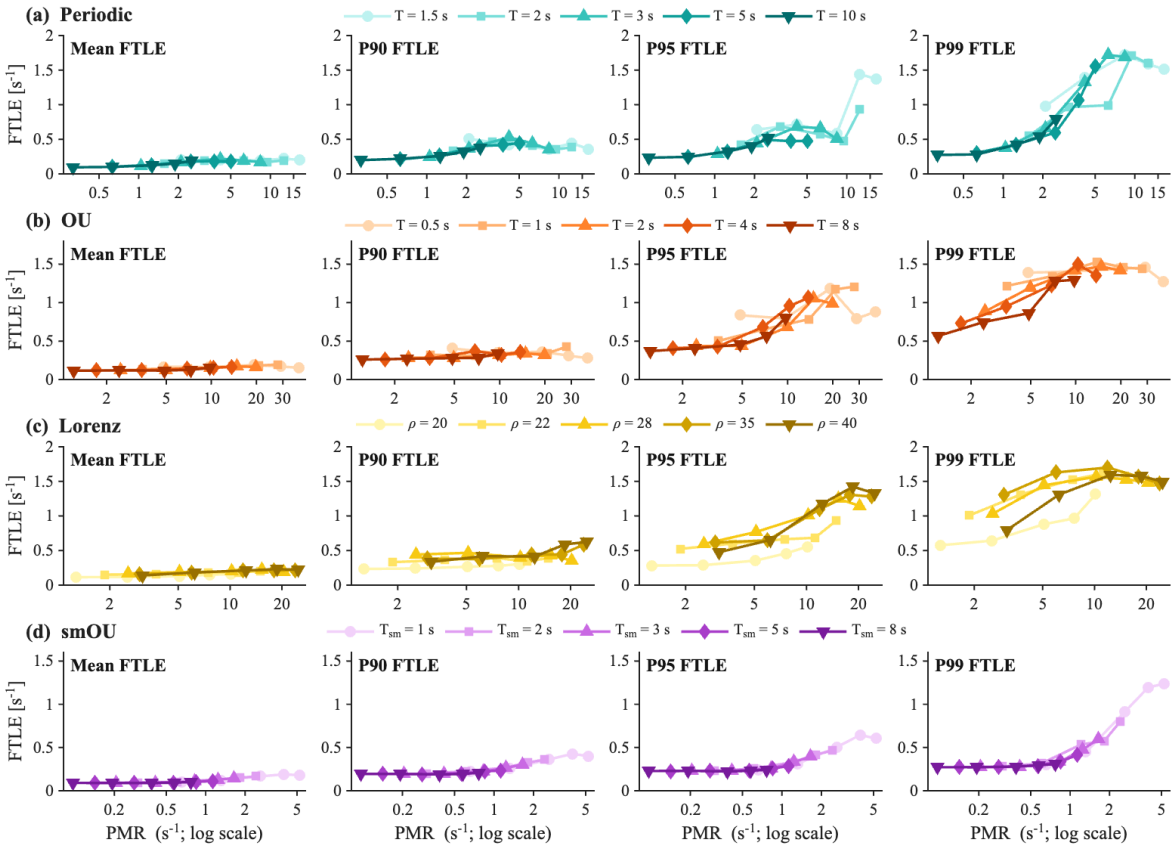


Fig. 6 Dependence of finite-time Lagrangian stretching on phase modulation rate (PMR). Rows correspond to the (a) Periodic, (b) OU, (c) Lorenz, and (d) smOU input families, and columns show the mean, P90, P95, and P99 FTLE, respectively. Colors and markers distinguish baseline cases within each family. FTLE generally increases with PMR, with a stronger response toward the upper tail despite local non-monotonic variations. PMR is shown on a logarithmic scale

are therefore characterized by a compact central region and a pronounced upper tail. This behavior is observed across the different input families.

The upper-tail statistics respond more strongly to modulation than the center of the distribution. As PMR increases, the Mean FTLE generally increases, while P95 and P99 exhibit larger changes. These differences indicate that the effect of temporal modulation varies across particle trajectories.

The broad upper tail reflects differences in the stretching accumulated along individual particle trajectories. High FTLE values are consistent with trajectories that accumulate favorable sequences of deformation and directional alignment over the finite integration interval. As discussed in Sect. 2.3, a larger strain-rate magnitude increases the available stretching capacity, whereas rotation and the evolution of the separation direction determine how much of this capacity is effectively accumulated.

The results therefore indicate that increasing PMR is expressed more strongly in the upper-tail FTLE statistics than in the distribution center, while most trajectories remain in the weak-to-moderate stretching regime. P95 and P99 are consequently more sensitive indicators of modulation-induced extreme Lagrangian response than the mean alone. This trajectory-dependent accumulation helps explain why changes in temporal modulation are more pronounced in the upper-tail FTLE statistics than in the distribution center.

4.4 OU modulation response

To further examine the modulation-dependent responses within the OU forcing family, five baseline correlation times $T_{\mathrm{OU}} = 0.5, 1, 2, 4, 8$ were

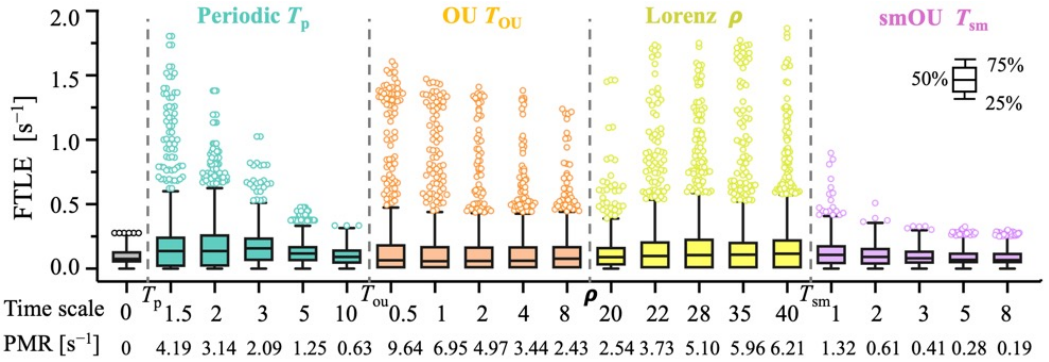


Fig. 7 FTLE distributions for the steady, Periodic, OU, Lorenz, and smOU cases. Boxes indicate the interquartile range (25th–75th percentiles), with the median shown inside each box; whiskers extend to the most extreme values within 1.5 times the interquartile range, and circles denote outliers

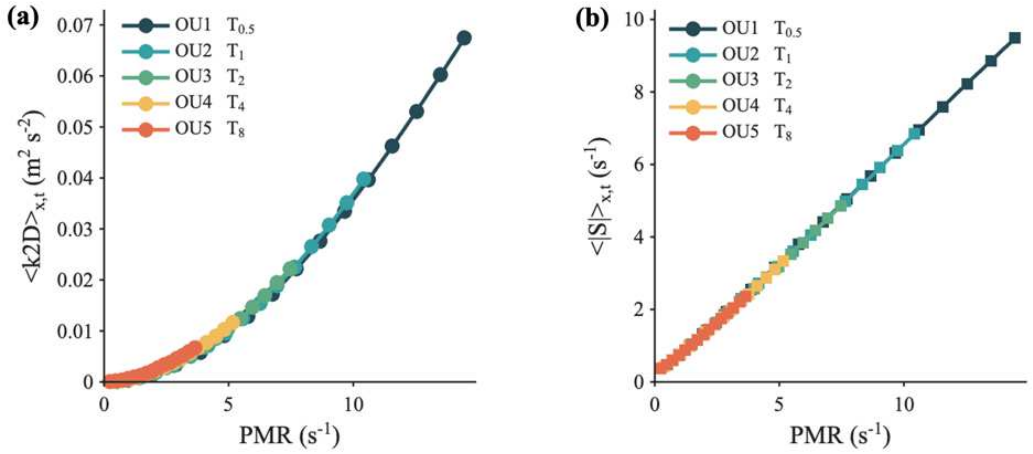


Fig. 8 Detailed Eulerian response within the OU forcing family. (a) Whole-field and time-averaged two-dimensional velocity-fluctuation energy, k_{2D}. (b) mean strain-rate magnitude, $|S|$, versus PMR for five OU baseline cases $T_{OU} = 0.5, 1, 2, 4, 8$

considered. For each baseline case, the input intensity multiplier I, defined in Sect. 4.1, was varied over a finer range from 0.1 to 1.5, and PMR was evaluated for each rescaled input signal. This allows the Eulerian and Lagrangian responses to be compared across different OU baseline conditions.

Fig. 8 presents the corresponding Eulerian responses. The whole-field velocity-fluctuation energy increases nonlinearly with PMR, whereas the mean strain-rate magnitude exhibits an approximately linear dependence. The five OU baseline cases follow closely aligned trends over their respective PMR ranges, particularly for the strain-rate response. This indicates that the relationship between PMR and Eulerian activity remains comparatively consistent despite differences in the baseline correlation time.

The corresponding Lagrangian responses are shown in Fig. 9, Mean, P90, P95, and P99 FTLE generally increase with PMR, with more pronounced changes in the upper-tail statistics. However, individual curves retain local plateaus, decreases, and fluctuations, particularly for P95 and P99. Unlike the comparatively smooth Eulerian responses, these variations indicate that the relationship between temporal modulation and finite-time Lagrangian stretching is less uniform.

The Pearson correlation analysis in Fig. 9(f) further reveals differences among the FTLE statistics. P95 exhibits consistently strong positive correlations with PMR across all five OU baseline

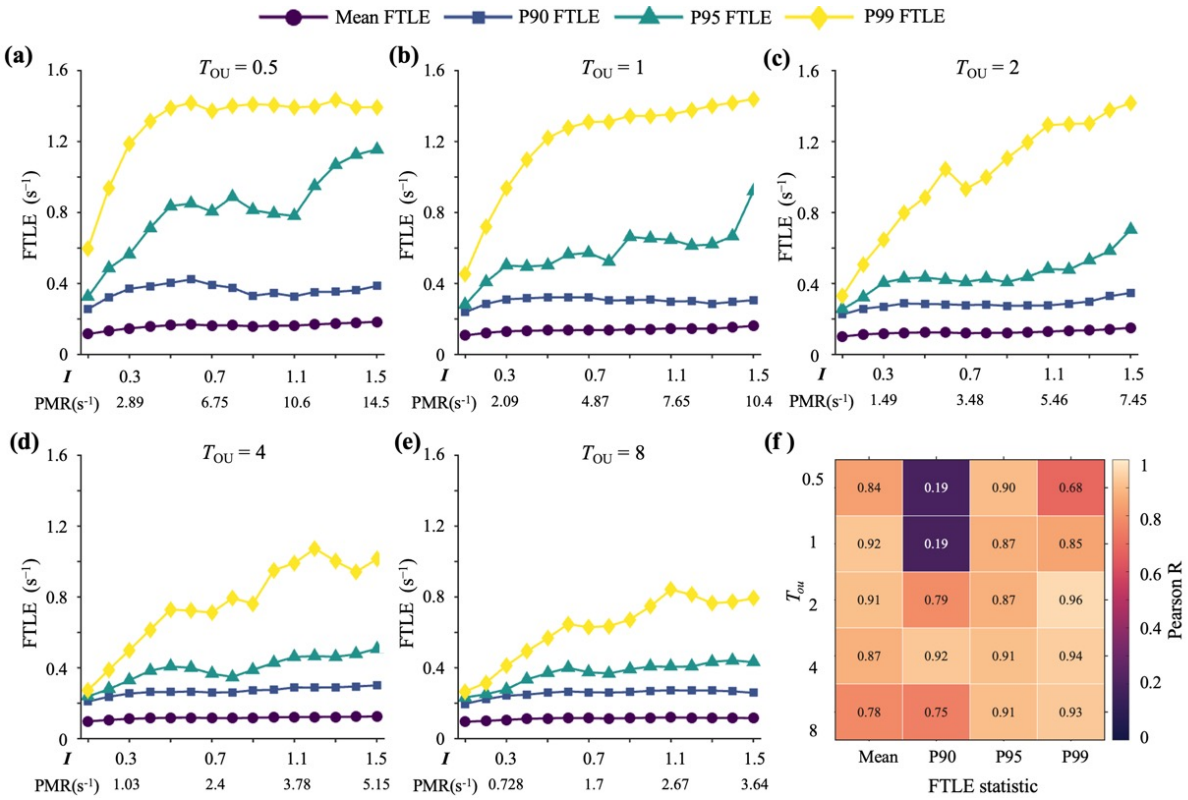


Fig. 9 Detailed Lagrangian response within the OU forcing family. Mean, P90, P95, and P99 FTLE versus I for (a–e) five OU baseline cases with $T_{\mathrm{OU}} = 0.5$, 1, 2, 4, 8, respectively. (f) Pearson correlations between PMR and the four FTLE statistics

cases $R = 0.87 - 0.91$, while P99 also shows predominantly strong positive correlations but with greater variation $R = 0.68 - 0.96$. The mean FTLE remains positively correlated with PMR, whereas P90 exhibits greater variability, including weak linear correlations $R = 0.19$ at $T_{\mathrm{OU}} = 0.5$ and 1 s. In these two cases, P90 increases initially but subsequently exhibits plateaus and local fluctuations, resulting in a weaker overall linear association with PMR. Faster temporal variations may also contribute to this behavior by modifying the accumulation of stretching through strain–rotation interactions and directional evolution. These results indicate that the linear association between PMR and finite-time stretching depends on both the baseline correlation time and the FTLE statistic considered, with P95 showing the most consistent positive correlation in the present OU scans.

Together with the results across the Periodic, Lorenz, and smOU families, the detailed OU analysis reveals a consistent modulation-dependent organization of Eulerian and Lagrangian responses. Increasing PMR is associated with a comparatively regular enhancement of Eulerian activity and an overall increase in finite-time Lagrangian stretching, while the latter retains statistical variability and local non-monotonicity. These findings demonstrate that PMR provides a common basis for organizing response trends across different temporal forcing conditions, while highlighting the distinct characteristics of Eulerian deformation and finite-time Lagrangian stretching.

5 Navier–Stokes CFD

5.1 CFD model and validation cases

The stream function model introduced above is a kinematic construction that satisfies incompressibility but does not explicitly enforce the Navier–Stokes momentum equation. An independent CFD calculation was therefore performed

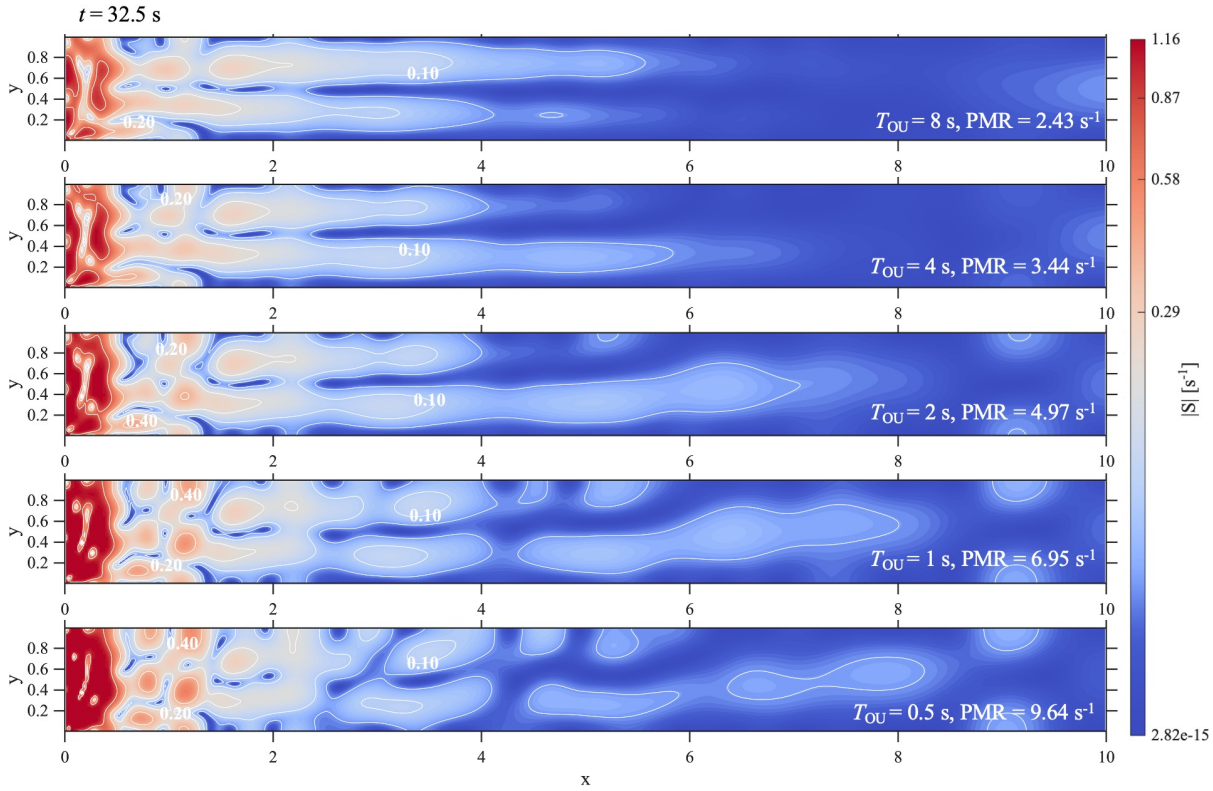


Fig. 10 Instantaneous Eulerian fields for the five OU cases at $t = 32.5\,\mathrm{s}$. Strain-rate magnitude $|S|(x, y)$ is shown for $T_{\mathrm{OU}} = 0.5$, 1, 2, 4, 8. White contour lines indicate selected strain-rate levels (s^{-1}). Stronger and more spatially extended deformation develops as T_{OU} decreases and PMR increases

to assess whether the modulation-dependent response obtained from the kinematic model is retained across the corresponding OU baseline cases when the velocity field is solved directly from the governing equations. The CFD simulations were conducted within the finite-volume framework of OpenFOAM [30] using the icoFoam solver for transient incompressible laminar flow. Pressure–velocity coupling was handled using the PISO (Pressure-Implicit with Splitting of Operators) algorithm [31]. No RANS or LES turbulence model was employed.

The two-dimensional incompressible Navier–Stokes equations are

$$\begin{aligned} \nabla \cdot \mathbf{u} &= 0, \\ \frac{\partial \mathbf{u}}{\partial t} + (\mathbf{u} \cdot \nabla)\,\mathbf{u} &= -\tfrac{1}{\rho}\nabla p + \nu \nabla^2 \mathbf{u}. \end{aligned} \tag{49}$$

Here, p denotes the physical pressure, ρ is the fluid density, and ν is the kinematic viscosity. The corresponding kinematic pressure $p_k = p/\rho$, stored as the field p, is used in OpenFOAM. The CFD domain uses the same geometry as the stream function model, with $L_x = 10$ and $L_y = 1$. The Reynolds number is $Re = \frac{U_0 L_y}{\nu} = 100$, chosen to retain inertial effects while maintaining a controlled laminar flow for comparison with the kinematic model, with $U_0 = 1$. A 400×100 grid is used. The internal CFD time step is 0.005, and the fields are sampled every 0.02 s up to $T = 50$ s. The simulations are transient, incompressible, and laminar, without RANS or LES modeling.

The temporal perturbation from the stream function model is mapped to the CFD inlet as

$$\begin{aligned} u_{\mathrm{in}}(y,t) &= U_0 + u'_{\psi}(0,y,t) \\ &\quad -\langle u'_{\psi}(0,y,t)\rangle_y, \\ v_{\mathrm{in}}(y,t) &= v'_{\psi}(0,y,t). \end{aligned} \tag{50}$$

This mapping preserves the temporal velocity perturbations while maintaining a constant mean streamwise inlet velocity and the no-penetration condition at the upper and lower boundaries. At the outlet, a zero-gradient condition is imposed for

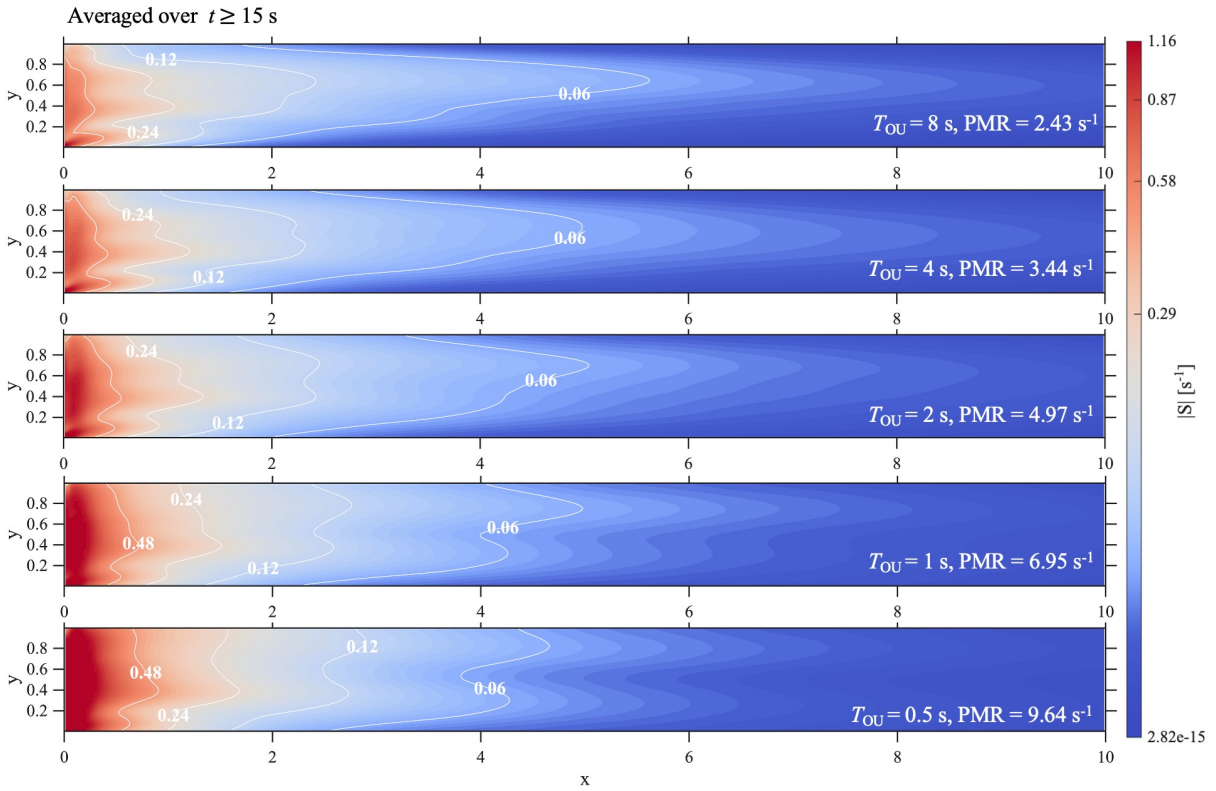


Fig. 11 Post-transient means Eulerian fields for the five OU cases. Strain-rate magnitude $|S|$, averaged over $t \geq 15$ s, is shown for $T_{\mathrm{OU}} = 0.5$, 1, 2, 4, 8. White contour lines indicate selected levels of the time-averaged strain-rate magnitude (s^{-1}).

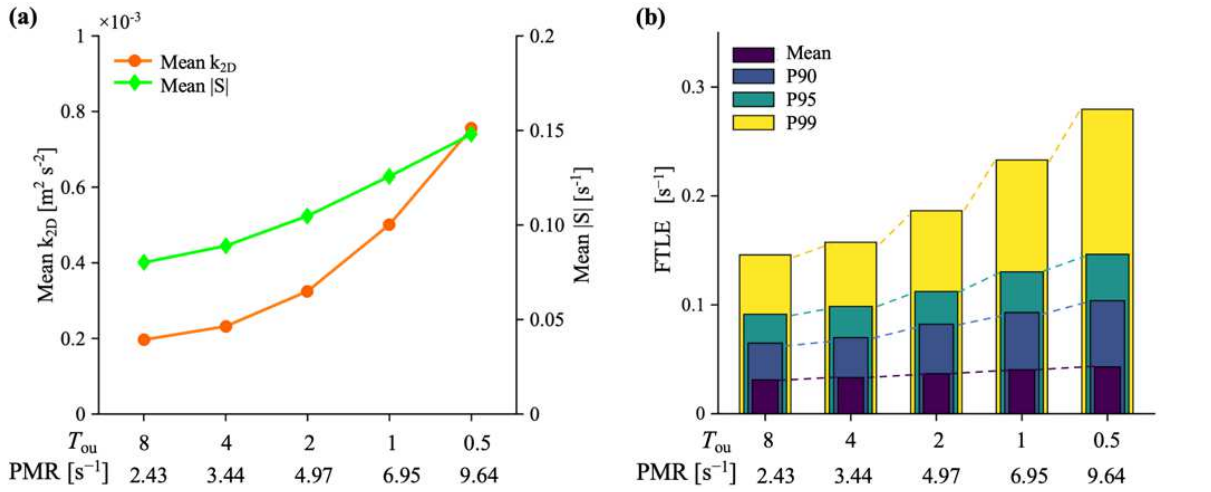


Fig. 12 CFD Eulerian and Lagrangian responses across the OU forcing sequence. (a) Whole-field and time-averaged k_{2D}, and $|S|$ for the steady reference and $T_{\mathrm{OU}} = 0.5$, 1, 2, 4, 8. (b) Mean, P90, P95, and P99 FTLE

velocity together with a fixed pressure. The upper and lower boundaries use slip conditions, consistent with the impermeable, non-no-slip boundaries of the kinematic stream-function model.

Six cases are considered for the CFD comparison: the steady reference case and five OU cases with $T_{\mathrm{OU}} = 0.5$, 1, 2, 4, 8, matching the corresponding cases used in the stream function model. This enables a direct case-by-case comparison of the modulation-dependent response between the kinematic and CFD models.

5.2 Validation

The CFD simulations reproduce the modulation-dependent response observed in the kinematic stream function model across the five OU baseline cases. As T_{OU} decreases from 8 to 0.5 s, corresponding to increasing PMR, both Eulerian activity and finite-time Lagrangian instability increase systematically.

The instantaneous Eulerian fields illustrate how this ordering emerges spatially. At $t = 32.5\ s$, the lower-PMR cases exhibit relatively localized deformation near the inlet, whereas decreasing T_{OU} produces stronger and more spatially extended strain-rate structures that persist farther downstream. The labeled strain-rate contours provide a common reference for comparing the location and spatial extent of deformation at selected $|S|$ (x, y) levels across the cases. These instantaneous fields demonstrate the increasing spatial extent of the modulation-induced flow response, although individual structures remain dependent on the instantaneous forcing state.

The same trend remains after temporal averaging. The fields averaged over the post-transient interval $t \geq 15\ s$ show a systematic increase in Eulerian activity with decreasing T_{OU}. The whole-field strain-rate magnitude $\langle |S| \rangle_t (x, y)$ increase across the OU sequence, demonstrating that the instantaneous differences persist at the statistical level. The labeled contours further distinguish the stronger near-inlet deformation from the weaker strain-rate regions extending downstream. The corresponding instantaneous and time-averaged $k_{2\mathrm{D}}$ fields exhibit the same qualitative progression.

The quantitative Eulerian statistics confirm this progression. As T_{OU} decreases from 8 to 0.5, both $\langle k_{2\mathrm{D}} \rangle_{x,y,t}$ and $\langle |S| \rangle_{x,y,t}$ increase systematically. The Lagrangian response follows the same ordering: the mean, P90, P95, and P99 FTLE all increase overall with decreasing T_{OU}, with the upper-tail statistics showing the strongest response.

Overall, the CFD results preserve the modulation-dependent ordering obtained from the kinematic model: increasing PMR is accompanied by stronger Eulerian activity and greater finite-time Lagrangian stretching. The reproduction of these trends in the Navier–Stokes simulations demonstrates that the modulation-dependent progression is retained beyond the prescribed kinematic stream-function model, establishing a consistent Eulerian and Lagrangian response across the two modeling approaches.

6 Discussion

6.1 Response hierarchy

The results reveal a clear hierarchy between Eulerian and Lagrangian responses to temporal modulation. Temporal variations of the input enter the velocity-gradient dynamics directly, and increasing PMR therefore produces a comparatively regular enhancement of Eulerian activity. By contrast, FTLE reflects deformation accumulated along particle trajectories and consequently exhibits greater variability and local non-monotonicity.

This distinction indicates that temporal modulation is transmitted relatively directly to local deformation, whereas its Lagrangian effect is filtered through finite-time trajectory dynamics. The Eulerian and Lagrangian responses are therefore related, but they operate at different dynamical levels.

6.2 Finite-time mechanism

The strain–rotation framework provides the mechanism for this difference. Strain determines the instantaneous stretching capacity, while rotation changes the particle-separation direction and therefore modifies its subsequent alignment with the extensional strain direction. FTLE consequently depends on both local deformation and the history of directional evolution.

The minimal linear model shows that increasing rotation at fixed strain can reduce the accumulated stretching and produce non-monotonic finite-time responses. This behavior is consistent with the local plateaus and decreases observed in the full simulations. The stronger responses of P95 and P99 further indicate that temporal modulation is expressed most strongly in trajectories undergoing large finite-time stretching.

6.3 Role of PMR

PMR provides a common measure for organizing the responses generated by different temporal inputs. Across the Periodic, OU, Lorenz, and smOU families, increasing PMR is consistently associated with stronger Eulerian activity and an overall increase in finite-time stretching. The detailed OU scans further show that this organization persists across different baseline correlation times.

PMR should therefore be interpreted as an organizing descriptor rather than a complete predictor of the flow response. It characterizes the intensity of temporal variation, while the remaining differences among forcing families reflect additional temporal structure and trajectory-dependent dynamics. Its main value is to provide a common coordinate for comparing qualitatively different forcing protocols.

6.4 Model consistency

The Navier–Stokes simulations extend the analysis beyond the prescribed kinematic flow. Across the steady reference and five OU cases, increasing PMR produces the same overall progression toward stronger Eulerian activity and larger FTLE statistics. Both the instantaneous fields and the statistical measures retain this ordering.

The agreement between the two modeling approaches indicates that the modulation-dependent response is not specific to the prescribed stream-function construction. Rather, the same overall dynamical sequence from temporal modulation to Eulerian deformation and subsequently to finite-time Lagrangian stretching is retained when the flow is governed by the incompressible Navier–Stokes equations. This cross-model consistency supports the broader applicability of the proposed response framework.

7 Conclusions

This study examined how temporal input modulation is transferred to Eulerian deformation and finite-time Lagrangian stretching in an unsteady incompressible flow. A phase-modulated stream-function framework was used to connect temporal forcing with velocity-gradient dynamics, and PMR was introduced to quantify the intensity of temporal modulation.

1. **Increasing PMR consistently enhances Eulerian activity.** Across the Periodic, OU, Lorenz, and smOU families, both velocity-fluctuation energy and strain-rate magnitude increase with PMR, indicating a comparatively direct response of local deformation to temporal modulation.
2. **Finite-time Lagrangian stretching exhibits a more complex response.** FTLE statistics increase overall with PMR but retain local plateaus, decreases, and fluctuations because the accumulated stretching depends on strain, rotation, separation-direction evolution, and trajectory history. P95 and P99 show stronger modulation sensitivity than the distribution center.
3. **PMR provides a common basis for organizing responses across different temporal inputs.** The refined OU scans confirm that the overall Eulerian and Lagrangian trends persist across different baseline correlation times, with P95 showing the most consistent positive correlation with PMR. PMR therefore serves as a compact organizing measure while retaining differences associated with forcing structure and finite-time trajectory dynamics.
4. **The modulation-dependent response is retained in Navier–Stokes simulations.** Across the steady reference and five OU cases, the CFD results reproduce the same overall progression toward stronger Eulerian activity and greater finite-time stretching with increasing PMR, supporting the transferability of the response framework beyond the prescribed kinematic model.

Overall, the results establish a hierarchical dynamical picture in which temporal modulation first modifies local Eulerian deformation, while the resulting finite-time Lagrangian stretching is

further shaped by directional evolution and trajectory history. PMR provides a compact measure for organizing this modulation-dependent response across different forcing conditions.

References

[1] Aref, H.: Stirring by chaotic advection. Journal of Fluid Mechanics **143**, 1–21 (1984) https://doi.org/10.1017/S0022112084001233

[2] Ottino, J.M.: Mixing, chaotic advection, and turbulence. Annual Review of Fluid Mechanics **22**, 207–254 (1990) https://doi.org/10.1146/annurev.fl.22.010190.001231

[3] Aref, H., *et al.*: Frontiers of chaotic advection. Reviews of Modern Physics **89**, 025007 (2017) https://doi.org/10.1103/RevModPhys.89.025007

[4] Solomon, T.H., Gollub, J.P.: Chaotic particle transport in time-dependent Rayleigh–Bénard convection. Physical Review A **38**, 6280–6286 (1988) https://doi.org/10.1103/PhysRevA.38.6280

[5] Voth, G.A., Haller, G., Gollub, J.P.: Experimental measurements of stretching fields in fluid mixing. Physical Review Letters **88**, 254501 (2002) https://doi.org/10.1103/PhysRevLett.88.254501

[6] Haller, G.: Distinguished material surfaces and coherent structures in three-dimensional fluid flows. Physica D: Nonlinear Phenomena **149**, 248–277 (2001) https://doi.org/10.1016/S0167-2789(00)00199-8

[7] Shadden, S.C., Lekien, F., Marsden, J.E.: Definition and properties of Lagrangian coherent structures from finite-time Lyapunov exponents in two-dimensional aperiodic flows. Physica D: Nonlinear Phenomena **212**, 271–304 (2005) https://doi.org/10.1016/j.physd.2005.10.007

[8] Haller, G.: Lagrangian coherent structures. Annual Review of Fluid Mechanics **47**, 137–162 (2015) https://doi.org/10.1146/annurev-fluid-010313-141322

[9] Girimaji, S.S., Pope, S.B.: Material-element deformation in isotropic turbulence. Journal of Fluid Mechanics **220**, 427–458 (1990) https://doi.org/10.1017/S0022112090003330

[10] Dresselhaus, E., Tabor, M.: The kinematics of stretching and alignment of material elements in general flow fields. Journal of Fluid Mechanics **236**, 415–444 (1992) https://doi.org/10.1017/S0022112092001460

[11] Lapeyre, G.: Characterization of finite-time Lyapunov exponents and vectors in two-dimensional turbulence. Chaos **12**, 688–698 (2002) https://doi.org/10.1063/1.1499395

[12] Thiffeault, J.-L.: Stretching and curvature of material lines in chaotic flows. Physica D: Nonlinear Phenomena **198**, 169–181 (2004) https://doi.org/10.1016/j.physd.2004.04.009

[13] Kelley, D.H., Ouellette, N.T.: Separating stretching from folding in fluid mixing. Nature Physics **7**, 477–480 (2011) https://doi.org/10.1038/nphys1941

[14] Aref, H., Balachandar, S.: Chaotic advection in a Stokes flow. Physics of Fluids **29**, 3515–3521 (1986) https://doi.org/10.1063/1.865828

[15] Rom-Kedar, V., Leonard, A., Wiggins, S.: An analytical study of transport, mixing and chaos in an unsteady vortical flow. Journal of Fluid Mechanics **214**, 347–394 (1990) https://doi.org/10.1017/S0022112090000167

[16] Kuczaj, A.K., Geurts, B.J., Lohse, D., Water, W.: Turbulence modification by periodically modulated scale-dependent forcing. Computers & Fluids **37**, 816–824 (2008) https://doi.org/10.1016/j.compfluid.2007.01.012

[17] Wang, J., Feng, L., Ottino, J.M., Lueptow, R.M.: Inertial effects on chaotic advection and mixing in a 2D cavity flow. Industrial & Engineering Chemistry Research **48**, 2436–2442 (2009) https://doi.org/10.1021/ie800404d

[18] Trefry, M.G., Lester, D.R., Metcalfe, G., Wu,

J.: Temporal fluctuations and poroelasticity can generate chaotic advection in natural groundwater systems. Water Resources Research **55**, 3347–3374 (2019) https://doi.org/10.1029/2018WR023864

[19] Wu, J., Lester, D., Trefry, M.G., Metcalfe, G.: Lagrangian coherent structures control solute dispersion in heterogeneous poroelastic media. Physical Review Fluids **9**, 044501 (2024) https://doi.org/10.1103/PhysRevFluids.9.044501

[20] Saporta-Katz, O., Mantel, N., Liran, R., Rom-Kedar, V., Gildor, H.: Northbound transport of the Mediterranean Outflow and the role of time-dependent chaotic advection. Geophysical Research Letters **51**, 2023–105662 (2024) https://doi.org/10.1029/2023GL105662

[21] Xu, A., Li, R.-Q., Xi, H.-D.: Temporal modulation on mixed convection in turbulent channels. Journal of Fluid Mechanics **1006**, 11 (2025) https://doi.org/10.1017/jfm.2025.22

[22] Tajima, S., Dentz, M.: Transient forcing in heterogeneous aquifers drives solute containment and chaotic mixing. Advances in Water Resources **203**, 105021 (2025) https://doi.org/10.1016/j.advwatres.2025.105021

[23] Kim, H., Ko, J., Son, D., Kim, J.-T.: Eulerian and Lagrangian analysis of pulsatile jet vortices in a closed-circuit platform. Physics of Fluids **38**, 061905 (2026) https://doi.org/10.1063/5.0325014

[24] Kraichnan, R.H.: Diffusion by a random velocity field. Physics of Fluids **13**, 22–31 (1970) https://doi.org/10.1063/1.1692799

[25] Fung, J.C.H., Hunt, J.C.R., Malik, N.A., Perkins, R.J.: Kinematic simulation of homogeneous turbulence by unsteady random Fourier modes. Journal of Fluid Mechanics **236**, 281–318 (1992) https://doi.org/10.1017/S0022112092001423

[26] Uhlenbeck, G.E., Ornstein, L.S.: On the theory of the Brownian motion. Physical Review **36**, 823–841 (1930) https://doi.org/10.1103/PhysRev.36.823

[27] Lorenz, E.N.: Deterministic nonperiodic flow. Journal of the Atmospheric Sciences **20**, 130–141 (1963) https://doi.org/10.1175/1520-0469(1963)020⟨0130:DNF⟩2.0.CO;2

[28] Lekien, F., Ross, S.D.: The computation of finite-time Lyapunov exponents on unstructured meshes and for non-Euclidean manifolds. Chaos **20**, 017505 (2010) https://doi.org/10.1063/1.3278516

[29] Rist, U., Weinschenk, M., Wenzel, C.: Investigation of Lagrangian Areas of Minimal Stretching (LAMS) in a turbulent boundary layer. Journal of Fluid Mechanics **970**, 31 (2023) https://doi.org/10.1017/jfm.2023.635

[30] Weller, H.G., Tabor, G., Jasak, H., Fureby, C.: A tensorial approach to computational continuum mechanics using object-oriented techniques. Computers in Physics **12**, 620–631 (1998) https://doi.org/10.1063/1.168744

[31] Issa, R.I.: Solution of the implicitly discretised fluid flow equations by operator-splitting. Journal of Computational Physics **62**, 40–65 (1986) https://doi.org/10.1016/0021-9991(86)90099-9

Acknowledgements. Weiqi Wen acknowledges stipend support from The University of Tokyo Fellowship (Todai Fellowship).

Statements and Declarations.

Funding. This work was supported by the Japan Society for the Promotion of Science (JSPS) Core-to-Core Program "Advanced core-to-core network for the physics of self-organizing active matter" (JPJSCCA20230002) and JSPS KAKENHI Grant Number JP25K15258.

Competing interests. The authors have no relevant financial or non-financial interests to disclose.

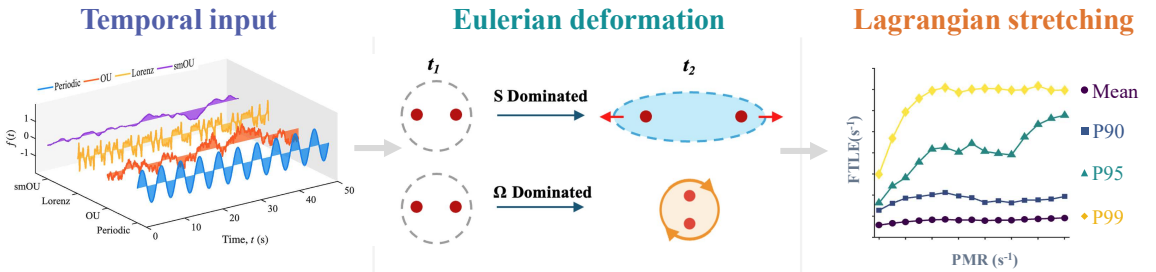
Author contributions. W.W. performed the theoretical derivation, numerical simulations, data

analysis, and manuscript preparation. H.K. supervised the research and reviewed the manuscript. Both authors contributed to the study conception and approved the final manuscript.

Data availability. The datasets and CFD simulation results generated during and/or analyzed during the current study are available from the corresponding author on reasonable request.

Code availability. The custom MATLAB scripts for signal generation, FTLE computation, and OpenFOAM setup files used during the current study are available from the corresponding author on reasonable request.

Temporal modulation and finite-time stretching



Periodic / OU / Lorenz / smOU

PMR = std (df / dt)

Different temporal structures

Strain stretches, rotation reorients

k_{2D} and |S|

Smooth increase with PMR

Stronger upper-tail response

FTLE distribution

Overall increase, local variability

Strain–rotation history shapes accumulated stretching